Climatology and ENSO-related interannual variability of gravity waves in the southern hemisphere subtropical stratosphere revealed by high-resolution AIRS observations

Kaoru Sato[1], Chikara Tsuchiya[14], M. Joan Alexander[2], and Lars Hoffmann[3]

Corresponding author: Kaoru Sato, Department of Earth and Planetary Science, The University of Tokyo, 7-3-1 Hongo, Bunkyo-ku, Tokyo, 113-0033, Japan. (kaoru@eps.s.u-tokyo.ac.jp)

[1]Department of Earth and Planetary Science, The University of Tokyo, Tokyo, Japan.

[2]NorthWest Research Associates, CoRA Office, Boulder, Colorado, USA.

[3]Jülich Supercomputing Centre, Forschungszentrum Jülich GmbH, Jülich, Germany.

[4]Now at Japan Coast Guard, Tokyo, Japan.

Abstract. A new temperature retrieval from Atmospheric Infrared Sounder with a fine horizontal resolution of 13.5 km was used to examine gravity wave (GW) characteristics in the austral summer at an altitude of 39 km in the subtropical stratosphere over eight years from 2003/2004−2010/2011. Using an S-transform method, GW components were extracted, and GW variances, horizontal wavenumbers and their orientations were determined at each grid point and time. Both climatology and interannual variability of the GW variance were large in the subtropical South Pacific. About 70 % of the interannual variation in the GW variance there was regressed to El Niño-Southern Oscillation (ENSO) index. The regression coefficient exhibits a geographical distribution similar to that of the precipitation. In contrast, the regression coefficient of the GW variance to the quasi-biennial oscillation of the equatorial lower stratosphere was not significant in the South Pacific. These results indicate that the interannual variability of GW variance in the South Pacific is controlled largely by the convective activity modulated by the ENSO. An interesting feature is that the GW variance is maximized slightly southward of the precipitation maximum. Possible mechanisms causing the latitudinal difference are (1) dense distribution of islands, which effectively radiate GWs with long vertical wavelengths, to the south of the precipitation maximum, (2) selective excitation of southward propagating GWs in the northward vertical wind shear in the troposphere, and (3) southward refraction of GWs in the latitudinal shear of background zonal wind in the stratosphere.

1. Introduction

It is well known that the meridional circulation in the middle atmosphere is driven by atmospheric waves, which maintain a temperature structure that is significantly different from that expected from radiative equilibrium [e.g., *Holton,* 1983]. Synoptic-scale waves are important to form the shallow branch of the Brewer-Dobson circulation (BDC), which is the meridional circulation in the stratosphere, both in the summer and winter hemispheres, while planetary waves are a main driver of the deep branch of the BDC in the winter hemisphere [e.g., *Plumb,* 2002]. In the mesosphere, gravity waves (GWs) are primary waves providing wave force to drive the meridional circulation [e.g., *Andrews et al.,* 1987]. However, GWs play an important role to drive the BDC as well, particularly for the summer hemispheric part of the winter circulation where dominant westward mean winds prohibit upward propagation of planetary waves, and for the shallow branches of the BDC through the westward forcing deposited in the weak wind layer above the middle latitude jet [*Okamoto et al.,* 2011; *Butchart,* 2012; *Stephan et al.,* submitted to the Journal of Atmospheric Science]. Studies using recently available high-resolution satellite observations and general circulation models suggest that the origins of GWs in the summer hemisphere are convection in the subtropical regions, particularly summer monsoon regions, while those in the winter hemisphere are topography and jet-front systems [*Sato et al.,* 2009; *Geller et al.,* 2013].

Satellites can detect GWs globally. However, the observable range of horizontal and vertical wavelengths by satellites are limited, and the limitations largely depend on the viewing geometry [*Alexander and Barnet,* 2007]. Limb-viewing satellite instruments such as the Limb Infrared Monitor of the Stratosphere (LIMS), the Cryogenic Infrared Spectrometers and Telescopes for the Atmosphere (CRISTA), and the High Resolution Dynamics Limb Sounder (HIRDLS) are able to detect GWs with relatively short vertical but long horizontal wavelengths. Nadir-viewing or sublimb-viewing satellite instruments and such as the Advanced Microwave Sounding Unit (AMSU) and the Atmospheric Infrared Sounder (AIRS) can observe GWs with relatively short horizontal but long vertical wavelengths. Such limitation in the detectable wavelength and/or frequency range is called as the observational filter [*Alexander,* 1998].

Several previous studies estimated absolute momentum flux associated with GWs using satellite data. *Geller et al.* [2013] conducted the first comparison among absolute momentum fluxes estimated using satellite, super pressure balloon, and radiosonde observations, those simulated by high resolution general circulation models (GCMs), and those parameterized in climate models. They showed that the parameterized GW momentum flux is largely different from those estimated by satellite observations and those of explicitly simulated in high resolution GCMs, and concluded that particularly, non-orographic GWs are not sufficiently well expressed in the GW parameterizations. It was also how such differences may cause systematic model biases that are observed in the jet structure in middle atmosphere models. Thus, the characteristics of GWs originating from nonorographic sources need be further investigated using high-resolution observations. According to the *Geller et al.* [2013] study, the GW momentum flux shows two peaks latitudinally: one is at subtropical latitudes in the summer hemisphere and the other is at high latitudes in the winter hemisphere. The former is considered to be due to GWs originating from monsoon convection [e.g. *Sato et al.,* 2009].

The horizontal distribution of GW variance at an altitude of 38 km with short horizontal and long vertical wavelengths has been investigated using high-horizontal resolution data from the Microwave Limb Sounder (MLS) [*Wu and Waters,* 1996; *McLandress et al.,* 2000; *Jiang et al.,* 2004]. MLS detected fluctuations with vertical wavelengths longer than 10 km. Hence part of the observed GW distributions, such as those around the polar night jet where strong winds refract waves to long vertical wavelengths, were attributable to the observational filter. However, the longitudinal distribution of GW variances in the summer subtropical regions may reflect the real nature of GWs, because large GW variance regions accord well with large outgoing longwave radiation (OLR), and because the background wind that can modify GW vertical wavelengths is zonally almost uniform. These GWs are likely originating from the convection in the subtropical region. Enhancement of the GW activity over the summer subtropical monsoon regions was also observed by HIRDLS, which can detect GWs with short vertical wavelengths and long horizontal wavelengths [*Wright and Gille,* 2011]. GWs originating from convection are expected to have short horizontal wavelengths comparable to individual convection and/or convective systems. Thus, it is important to examine nadir-view satellite observation data as well. Currently, AIRS has the highest horizontal resolution, that is 13.5 km across and 18 km along the satellite orbit at nadir. Several previous studies using the AIRS radiance data examined the GW characteristics by applying a wavelet analysis method for a specific height level in the stratosphere [*Alexander and Barnet,* 2007; *Alexander and Teitelbaum,* 2007; 2011]. In this paper, we analyze high-resolution AIRS temperature data from a new retrieval [*Hoffmann and Alexander,* 2009] focusing on GWs in the subtropical region.

There are few studies on the interannual and intraseasonal variability of the GW activity except for the relation to the equatorial quasi-biennial oscillation (QBO), using radiosondes [*Sato et al.,* 1994; *Sato and Dunkerton,* 1997], satellites [*Ern and Preusse*, 2009; *Gong et al.,* 2012; *John and Kumar,* 2012; *Zhang et al.,* 2012], and high resolution numerical models [*Kawatani et al.,* 2010; *Evan et al.,* 2012]. However, the interannual and intraseasonal variability of GW variance can be affected by other dominant phenomena in the tropical and subtropical regions such as the El Niño-Southern Oscillation (ENSO) and Madden-Julian Oscillation (MJO). These phenomena have characteristic horizontal structure. As AIRS started its observation in 2002, the observation duration is sufficient to examine such interannual and intra-seasonal variations. In the present study, AIRS data over nine years from 2003 to 2011 were used to examine the climatology of GWs in the summer subtropical region and the interannual variability of GWs in terms of ENSO. The intraseasonal variability in terms of MJO is investigated in a companion paper [*Tsuchiya et al.,* submitted to the Journal of Geophysical Research].

In section 2, details of the AIRS observation data and the method of analysis are described. The climatology of GWs in the tropical and subtropical regions in summer is presented in section 3. In section 4, the interannual variability of GWs and its relation to ENSO is shown focusing on the SH subtropical region. In section 5, modulation of GWs by the QBO as another factor causing the interannual variability, and possible mechanism of the latitudinal difference between GW and convection maxima that is elucidated in the present study are also examined and discussed. Summary and concluding remarks are given in section 6.

2. Data description and method of analysis

2.1. Data description

AIRS *[Aumann et al.,* 2003] is one of six instruments onboard the Aqua satellite [*Parkinson,* 2003]. Aqua was launched on May 4, 2002. It has a Sun-synchronous nearly polar orbit with 98° inclination at 705 km altitude. Aqua crosses the equator at 01:30 (descending orbit) and 13:30 (ascending orbit) local time.

AIRS measures the thermal emissions from atmospheric constituents in the nadir and sub-limb directions. The scan angle across the measurement track is ±49.5°, corresponding to a distance on the ground of 1765 km [*Hoffmann et al.,* 2013]. Each across-track scan consists of 90 foot prints. The extent of a granule, which is consisted of 135 scans, is about 2400 km along the track. Kernel functions of CO_2 channels with radiances of 15 and 4.3 μm typically have a peak in the stratosphere and a depth of about 12 km [*Alexander and Barnet,* 2007; *Hoffmann and Alexander,* 2009].

The AIRS operational level 2 temperature product has a horizontal resolution coarser than the original radiance measurements by a factor of 3×3, which corresponds to the horizontal resolution of Advanced Microwave Sounding Unit (AMSU) on board Aqua. However, the level 2 temperature data may be not sufficient to detect such short horizontal wavelengths as convectively-generated GWs have. To overcome this shortage, *Hoffmann and Alexander* [2009] developed a new retrieval of atmospheric temperature, which provides data with a native high resolution of the AIRS radiance measurements. They used 23 channels of 4.3 μm radiance and 12 channels of 15 μm radiance for retrievals at the nighttime when the solar zenith angle is larger than 96°, while only 12 channels of 15 μm radiance are used for retrievals at the daytime, because the assumption of local thermodynamic equilibrium for 4.3 μm radiance is not valid. Thus, the noise level of the retrievals at nighttime is lower than that at daytime. With this reason, the present study used the new retrieval of temperature at the nighttime only. In addition, the noise of the AIRS high resolution retrieval of temperature is minimized for an altitude range 25–45 km. Following previous studies, this study focused on a specific height level of 39 km approximately corresponding to 3 hPa. Vertical resolution is about 9 km at that level. Analyzed time period is nine years from 2003 to 2011. A validation of the new AIRS retrieval is presented by *Meyer and Hoffmann* [2014].

A reanalysis data, NASA's Modern-Era Retrospective Analysis for Research and Applications (MERRA) [*Rienecker et al.,* 2011] is used for the analysis of the background field of GWs. MERRA data is generated with the Goddard Earth Observing System (GEOS) atmospheric model and data assimilation system (DAS) where AIRS data is also assimilated. Although the original MERRA data is available three hourly, daily mean temperature and horizontal wind values are used for the analysis. The ocean fraction at each grid point in the numerical model used for MERRA is also used to see the surface condition.

In addition, we used daily 1×1° gridded precipitation data from the Global Precipitation Climatology Project (GPCP) version 1.2 [*Huffman et al.,* 2001] as an index of convection. The NINO.3 index, which is defined as SST anomalies averaged over the region which is 5°S to 5°N and 150°W to 90°W, from Japan Meteorological Agency (http://www.data.jma.go.jp/gmd/cpd/data/elnino/nino3irm.html) is used as an ENSO time series.

2.2. Method of analysis

In this section, the method used in the present study to analyze the horizontal propagation characteristics of GWs is described. S-transform [*Stockwell et al.,* 1996] is a one-dimensional wavelet-type analysis and is suitable for the estimation of local characteristics of GWs. Several previous studies [*Alexander and Barnet,* 2007; *Alexander et al.,* 2008; *Alexander et al.,* 2009; *Alexander and Grimsdell,* 2013] applied the S-transform to the satellite data of AIRS and HIRDLS to detect localized GW packets.

First, a large-scale field was obtained as the data scans of temperature across the orbit regressed to a second-order polynomial function and smoothed by the 31-point running mean along the orbit. The deviation of the original data from the large-scale field was designated as the GW components. Original sampling interval of the data scans across the orbit varies from 13.5 km at nadir to 39.6 km at its edge. So as to make the analysis easier, the GW components are interpolated at the same interval of 13.5 km by a spline fit across the track. As a consequence, the number of data series across the track becomes 130.

GW parameters were estimated using an S-transform method. So as to obtain statistically stable S-transform spectra, a window function, which has a cosine shape at both ends for one tenth of the total length, was multiplied to the GW data series. The S-transform spectra were calculated at respective GW data series across the track. Cross spectra for respective two adjacent data series were obtained using the S-transform spectra.

A wavenumber vector (k, l) of the GWs is estimated at each grid point. Here, k and l are the wavenumber components in the direction of the data series (i.e., across the track) and perpendicular to that direction, respectively. The wavenumber k is determined as the wavenumber at which the magnitude of the cross spectral density is maximized in the meaningful wavenumber range. Here the meaningful wavenumber range was estimated at $2\pi/(70\text{ km})$ to $2\pi/(700\text{ km})$ based on an analysis of noise spectra (see Appendix for details). The wavenumber component across the data series (i.e., along the track), l', is estimated from the phase shift of the cross spectra at k. Note that l' is different from l, because the two data series which are respectively across and along the track are not right-angled. The angle between the two data series a is shown in Figure 1a as a function of the latitude. The relation among k, l, l', and a is illustrated in Figure 1b. The wavenumber component l is estimated using k, l', and a as

$$l = \frac{l' - k\cos(a)}{\sin(a)}. \quad (1)$$

Because the window function applied to the data series, the region where the wavenumber vector data are obtained consists of central 90 grid points out of the total 130 grid points. Similar analysis was performed by applying the S-transform to the data series "along" the track with a length of 196, and the estimation of wavenumber vector was made for the central 135 grid points. Note that the former and latter analyses provide better estimates for waves with $|l| < |k|$ and $|l| > |k|$, respectively.

In this way, we obtained a pair of horizontal wavenumber vectors for each grid point for the same GW, i.e., one from the two adjacent data series across the track and the other from that along the track. Through tests with idealized wave patterns, a better estimate of (k, l) vector was selected with a criteria based on the angle of the horizontal wavenumber vector relative to the track, φ. For reference, k and l can fall in the range of -90° to 90° for both across track and along track estimates, where a positive (negative) φ value means an angle counter-clockwise (clockwise) from the track direction. We selected the estimate from the along-track data series when -45°<φ<45°, and that from the across-track one when φ ≤-45° or φ ≥45°. The direction of the horizontal wavenumber vector in the Cartesian coordinate, φ_{h}, is then estimated using the track direction, φ_0, as $\varphi_{\mathrm{h}} = \varphi + \varphi_0$. Positive φ_{h} values show angles with counter-clockwise rotation from the eastward direction. Note that there is an ambiguity of 180° in φ_{h}. According to a GW-resolving general circulation model study by *Sato et al.* [2009], dominant GWs tend to have negative (positive) vertical flux of zonal momentum in the eastward (westward) background wind. This means that the zonal component of horizontal wavenumber vector has opposite sign to the background zonal wind. Thus, based on this fact, we determined the direction of horizontal wavenumber using the zonal wind from MERRA at each grid point. The horizontal wavelength is calculated as $\lambda_{\mathrm{h}} = 2\pi/(k^2 + l^2)^{\frac{1}{2}}$.

GW amplitude squared was estimated as the absolute value of the cross spectra at k with a unit of K^2, which is hereafter referred to as the GW variance. Note that this GW variance is equal to twice as much as conventional variance.

In addition, it was seen that data were quite noisy and temperature perturbation signals were quite weak in the regions with weak background winds. This is probably because in such weak background winds, vertical wavelengths of GWs are not sufficiently long to be detected by AIRS. Thus, we simply omitted the data in regions where the background wind slower than 10 m s^{-1} for the analysis. This threshold for the background wind is somewhat arbitrary, however it was confirmed that the results are not sensitive to slight changes of the threshold.

3. Climatology of GWs in the summer subtropics

Figures 2a and 2b show maps of the climatology of GW variance in the summer subtropics for the Southern Hemisphere (SH) averaged over December to February (DJF) and for the Northern Hemisphere (NH) over June to August (JJA), respectively. The GW variances are large over continents such as South Africa, Australia, South America, North Africa, South and Southeast Asia, and North America and over the western to central South Pacific. This feature is consistent with MLS observations [*McLandress et al.,* 2000; *Jiang et al.,* 2004].

Figure 2c (2d) shows maps of the standard deviation of seasonal mean GW variance showing interannual variability in the SH (NH). The numbers of years to obtain the interannual variability is eight and nine for Figures 2c and 2d, respectively.

An interesting feature is that the interannual variability of the GW variance in the summer subtropics is larger in the SH than that in the NH, although the climatological GW variances are comparable. The standard deviation of the DJF-mean GW variance in the Australian monsoon region amounts to about 20 % of the climatology (Figure 2c), while in JJA Asian monsoon region it is about 12 % (Figure 2d). Thus, in the following, we mainly analyze the climatology and interannual variability of DJF-mean GW characteristics in SH subtropics.

Figure 3 shows DJF-mean climatology of (a) precipitation and zonal winds at 100 hPa, (b) GW variance and zonal winds at 3 hPa, (c) GW horizontal wavelength averaged with a weight of the GW variance, and (d) GW horizontal wavenumber direction φ_h averaged with a weight of the GW variance in the SH tropical and subtropical region. The South Pacific Convergence Zone (SPCZ) is defined as the latitudes of the precipitation maxima for respective bins from 150°E−140°W and denoted by a red curve in all maps of Figure 3.

As expected, the GW variance maxima are observed in strong precipitation regions such as in South Africa, Australia, and South America continents and in the South Pacific. This indicates that the GWs at 39 km observed by AIRS are originating from strong convection in the troposphere. It is interesting that the GW variance maxima are located southward of the precipitation maxima by a few degrees at respective longitudes. Similar difference in the locations of precipitation and GW variance maxima is also seen in South Africa and South America.

The zonal wind at 3 hPa is mainly zonally uniform in Figure 3b, although it is slightly stronger southward of the SPCZ. This fact indicates that the characteristic longitudinal distribution of GW variance observed in Figure 3b (or Figure 2a) is not solely due to the observational filter of AIRS, but is reflecting true differences in GW properties. The mean GW horizontal wavelengths are long (>200 km) over southeastern Africa, Australia, and southwestern America where the GW activity is high, while those in the other regions are ~150 km (Figure 3c). The mean horizontal wavenumber direction is eastward or slightly southward in most regions (Figure 3d). The direction tends to more southward to the west of the precipitation.

4. ENSO-related interannual variability of GW variance

As a possible cause of the GW interannual variability observed by AIRS in the austral summer season, we examined the relation with ENSO. DJF-mean GW variance and precipitation were made in respective years and binned at each 2.5°×10° latitude-longitude box area. To see the interannual variability of ENSO, the NINO.3 index is used (Figure 4) (e.g. *Trenberth,* 1997). Note that a five-monthly mean was applied to the NINO.3 index by its definition. Values of the NINO.3 index in January of 2004 to 2011 were used as a reference time series for our analysis. It is seen that DJF periods of 2003/2004, 2004/2005, 2006/2007 and 2009/2010 (2005/2006, 2007/2008, 2008/2009 and 2010/2011) are in El Niño (La Niña) or similar conditions, which are hereafter referred to as the El Niño (La Niña) years.

Figures 5a (5b) shows correlation coefficients of the DJF-mean precipitation (GW variance) with the NINO.3 index. Figures 5c (5d) represents regression coefficients of the DJF-mean precipitation (GW variance) to the NINO.3 index in the region where the magnitude of correlation coefficients with the NINO.3 index is larger than 0.62 corresponding to a confidence level of 90%. Positive correlation and regression coefficient values indicate an increase in the precipitation and GW variance in the El Niño years.

Magnitudes of the correlation coefficients are greater than 0.83 over the subtropical South Pacific for both precipitation and GW variance. The regressed component accounts for about 70% of the GW interannual variability at most. The precipitation has positive regression and correlation coefficients eastward of SPCZ and in the central equatorial South Pacific, and negative regression and correlation coefficients westward of SPCZ and in the eastern South Indian Ocean. The coefficients for the GW variance exhibit similar distributions. An exception is seen at the Maritime Continent where the correlation and regression coefficients are significantly negative for the precipitation, while they are small for the GW variance. Thus, further analysis is made for three regions where characteristic interannual variability of the GW variance is observed, synchronized with ENSO: (A) the equatorial western South Pacific region (0°S to 10°S, 150°E to 150°W), (B) the subtropical region (10°S to 30°S, 150°E to 110°W) to the east of the SPCZ, and (C) the subtropical region to the west of the SPCZ that are denoted in Figure 5c

Such characteristic modulation of the GW variance by ENSO is likely due to modulation of GW sources (i.e. convection). However, we need to scrutinize carefully the possibility of virtual modulation by the observational filter. As horizontal wavenumber vectors are oriented mainly zonally (Figure 3d), GWs tend to have longer vertical wavelengths in stronger zonal winds. Thus, even if the horizontal phase speed spectra of GWs propagating into the middle stratosphere are the same, the GW variance observed by AIRS may exhibit virtual interannual variability by inter-annually varying background zonal winds.

To examine this possibility, we calculated DJF-mean background wind zonal wind at 3 hPa for respective years and averaged over respective A, B, and C regions. Results are shown in Figure 6 together with the time series of DJF-mean GW variance and precipitation averaged over respective regions. Regional dependence is clear for the GW variance and precipitation: both the GW variance and precipitation values are large (small) in the A and C regions and small (large) in the B region in the El Niño years except 2003/2004 (the La Niña years). In contrast, the mean zonal wind exhibits similar variation for all regions and does not seem to be modulated much by ENSO. Thus, we can exclude the possibility of the observational filter alone causing the interannual variability observed in the GW variance. It is therefore concluded that the interannual variability of stratospheric GWs in the SH summer subtropical region is largely due to the modulation of tropical convective GW sources by ENSO.

The regression to the NINO.3 index is also performed for the mean horizontal wavelengths and the horizontal wavenumber direction (Figure 7). The correlation and regression coefficients for the horizontal wavelengths exhibit similar patterns to those for the GW variance (Figures 5b and 5d): They are largely positive in the A and C regions and negative in the B region. The rate of change in the horizontal wavelength is about 20 km per 1 K NINO.3 SST at most. In contrast, the regressed pattern of horizontal wavenumber direction shows different features: Significant negative correlation and regression coefficients are observed along the SPCZ. This means that the GWs over the SPCZ propagate slightly more southward relative to the mean wind in the El Niño phase than in the La Niña phase. The rate of change in the direction is about 2° per 1 K NINO.3 SST.

As described in section 3, the DJF-mean GW variance climatology is maximized slightly to the south of the precipitation maximum (Figures 3a and 3b). This feature is further examined by making a composite separately for the El Niño years and for the La Niña years. Figure 8a shows composite profiles of the GW variance (black) and precipitation (blue) as a function of the latitude relative to the climatological SPCZ latitude that are averaged over longitudes from 150°E−150°W for all years (i.e., climatology), while Figures 8b and 8c represent the same composite profiles but for the El Niño and La Niña years, respectively. A profile of a mean ocean fraction in each grid box for the same longitude region is also plotted by a green curve in Figure 8, which will be referred to in the discussion in section 5.2.

The precipitation maximum shifts northward (southward) in the El Niño (La Niña) years compared with the climatology. However, it is commonly seen for both phases that the GW variance is maximized southward of the precipitation maximum. It is interesting that the latitudinal difference between the precipitation and GW variance maxima is larger in the El Niño years than in the La Niña years. This feature is at least qualitatively consistent with the fact that the mean horizontal wavenumber vector direction is more southward in the El Niño years (Figures 7b and 7d).

5. Discussions

5.1 Possibility of interannual variability modulation by the QBO

As described in section 1, the interannual variability of stratospheric GWs in the tropical region has been discussed in terms of the QBO in previous studies. It seems, however, that the QBO does not largely modulate the interannual variability of the GWs observed by AIRS over this subtropical South Pacific region, as is shown below.

As a QBO index, we used a time series of DJF-mean zonal-mean zonal wind at 10 hPa at the equator from MERRA. Figure 9a and 9b respectively show correlation and regression coefficients between the GW variance at respective locations and the QBO index. Regression coefficients of the GW variance time series to the QBO index are only shown in regions where the correlation coefficient magnitudes are greater than 0.62 corresponding to a confidence level of 90%. Significant modulation by the QBO is observed in longitudes from 120°W eastward to 60°E at latitudes lower than 10°S. The negatively large regression coefficients in this region mean that the GW variances are larger in the westward phase of the QBO at 10 hPa than the eastward phase. In contrast, significant modulation by the QBO is not observed in the west and central South Pacific region even near the equator which is the focus in the present study. Similar results were obtained for the correlation and regression analysis performed using zonal-mean zonal wind at the equator at 30, 40, 50, and 70 hPa (not shown). Thus, this result also strongly suggests that the interannual variability of stratospheric GWs over the western and central parts of the subtropical South Pacific in austral summer is largely affected by ENSO.

5.2. Possible mechanisms of latitudinal difference between GW and convection maxima

An interesting result from the analysis of climatology in Section 4 is that the DJF-mean GW variance takes its maximum southward of the precipitation maximum by about 3°. In this section, we discuss three possible mechanisms causing the latitudinal gap of stratospheric GWs and tropical convection in the South Pacific. They are (1) island distribution, (2) selective excitation of southward propagating waves in the troposphere, and (3) southward refraction due to background wind shear in the stratosphere. Other mechanisms and a combination of these mechanisms are also discussed.

5.2.1 Island distribution

Island distribution may affect the GW climatology because the occurrence frequency of deep convection over the land is higher than that over the ocean [*Takayabu,* 2002]. Thus, it is expected that GWs with long vertical wavelengths are generated more effectively over the islands. Such GWs with long vertical wavelengths have fast intrinsic phase speed and hence less frequently encounter their critical levels compared with those with short vertical wavelengths. In addition, such GWs with long wavelengths are more easily detectable by AIRS.

As a proxy of the existence of islands, we used mean ocean fraction for each bin, which is hereafter referred to as MOF. A map of MOF is plotted in Figure 10a. MOF values are zero over continents and one over oceans by its definition. Small but nonzero MOF values are observed around and in particular southward of SPCZ indicating that a number of islands and/or islands with large areas are distributed there.

Figure 10b shows a histogram as a function of the DJF-mean climatology of GW variance versus that of precipitation for a region of (0°S−30°S, 160°E−160°W) which is denoted by a rectangle on the map in Figure 10a. It is clear that the two quantities are positively correlated. Figure 10c shows the mean of MOF values at respective bins of this plot by the same color scale as used for Figure 10a. The mean MOF values are smaller at larger GW variance for a particular precipitation value. This result indicates that GWs are effectively generated from convection over islands.

In Figure 8, composite MOF values were shown as a function of the latitude relative to the climatological SPCZ. It is seen for the climatology in Figure 8a that the MOF takes its minimum slightly southward of the precipitation maximum and slightly northward of the GW variance maximum. It is also seen from Figures 8b and 8c that the GW variance maximum does not move much and remains close to the MOF minimum, although latitudinal movement of the precipitation maximum is largely depending on the ENSO phase. This result is consistent with our inference that convection over islands effectively generates GWs with long vertical wavelengths, and suggests that the island distribution is partly attributable to the difference in the dominant latitude between the observed GW variance and precipitation. In addition, it is worth noting that the diurnal cycle of convection near islands has a peak in evening [*Mori et al.,* 2004; *Ichikawa et al.,* 2008], while convection over the tropical Pacific and Atlantic Oceans is maximized in the morning [*Serra and McPhaden,* 2004]. Night time observations by AIRS which are used in the present study maybe more apt to detect GWs originating from convection near islands rather than those over the ocean. However, as the MOF minimum is always located slightly northward of the GW variance maximum (Figures 8a, 8b and 8c), additional mechanisms causing southward shift of the GW variance maximum are necessary.

5.2.2. Selective excitation of GWs in the background wind shear

Beres et al. [2002] showed from a series of numerical simulation using a two-dimensional model that GWs propagating opposite to the upper tropospheric wind shear are effectively excited by convection in squall lines. Figure 11a shows vertical profiles of composite meridional winds for longitudes of 160°E−160°W as a function of the latitude relative to SPCZ. Composites of precipitation and GW variance for the same longitude region are respectively shown in Figures 12b and 12c as a function of the latitude relative to the SPCZ. As was also shown in Figure 8a, the latitude of GW variance maximum is observed southward of the precipitation maximum by 3°.

Northward wind is observed in the upper troposphere with a maximum around 200 hPa and hence the vertical wind shear in the troposphere is northward. This wind structure suggests that southward propagating GWs should be more effectively excited from the SPCZ. This implication is qualitatively consistent with the relative location of the GW variance and precipitation maxima.

A rough but quantitative estimation is made for a possible latitudinal propagation distance of GWs using typical wave parameters obtained from the S-transform analysis: The mean horizontal wavenumber $k_{\mathrm{h}} = 2\pi/(225\ \mathrm{km})$ (Figure 3c) and a mean horizontal wavenumber direction of −4.5° (Figure 3d) around the location (15°S, 180°E) near the SPCZ. A typical observable vertical wavenumber m is assumed as $2\pi/(15\ \mathrm{km})$. The inertial frequency f at 15°S is $2\pi/(46.4\ \mathrm{h})$ and a typical stratospheric Brunt-Väisälä frequency N is assumed as $2\pi/(5\ \mathrm{min})$. From the linear theory of non-hydrostatic internal inertia-gravity wave, vertical ($c_{\mathrm{g}z}$) and meridional group velocity components ($c_{\mathrm{g}y}$) are expressed as;

$$c_{\mathrm{g}z} = \frac{-k_{\mathrm{h}}^2 m (N^2 - f^2)}{(m^2 + k_{\mathrm{h}}^2)^{\frac{3}{2}} (N^2 k_{\mathrm{h}}^2 + f^2 m^2)^{\frac{1}{2}}}, \tag{2}$$

$$c_{\mathrm{g}y} = \frac{k_y m^2}{(m^2 + k_{\mathrm{h}}^2)^{\frac{3}{2}}} \frac{N^2 - f^2}{(N^2 k_{\mathrm{h}}^2 + f^2 m^2)^{\frac{1}{2}}} = \frac{k_{\mathrm{h}} \sin\phi_{\mathrm{h}}\, m^2}{(m^2 + k_{\mathrm{h}}^2)^{\frac{3}{2}}} \frac{N^2 - f^2}{(N^2 k_{\mathrm{h}}^2 + f^2 m^2)^{\frac{1}{2}}}, \tag{3}$$

where k_y is meridional wavenumber ($\equiv k_{\mathrm{h}} \sin \phi_{\mathrm{h}}$), and estimated using the above-mentioned parameters at c_{gz} =3.31 m s^{-1} and c_{gy} =3.89 m s^{-1}. Thus, the time period needed for propagation from the upper troposphere (z = 9 km) to the stratosphere (z = 39 km) is estimated at about 2.52 h and the latitudinal distance over which the GWs migrate is 35.3 km. This value is not sufficient to explain the observed distance of 3° (~330 km). Thus, a preference for excitation of southward waves is not the only mechanism causing the large latitudinal distance between the GW variance and precipitation maxima, although it is qualitatively consistent.

5.2.3 Refraction due to the latitudinal gradient of zonal wind

GWs tend to propagate meridionally by refraction in a background zonal wind having latitudinal shear [*Dunkerton,* 1984; *Sato et al.,* 2009]. Meridional cross sections of the mean zonal wind are shown for two longitudes of 160°E and 160°W (Figure 12) instead of a composite, because changes largely depend on longitude (see Figure 3a). The latitudinal gradient of zonal wind, $\partial U/\partial y$, is mainly positive in the stratosphere in the latitude range between the GW variance and precipitation maxima. Assuming that the zonal wavenumber (k_x) is positive in the westward background wind, the k_y tendency is negative from the ray tracing theorem,

$$\frac{\mathrm{d}k_y}{\mathrm{d}t} = -k_x \frac{\partial U}{\partial y} \tag{4}$$

This means that the GW packets would tend to propagate southward. This fact is at least qualitatively consistent with the difference in the latitude between the GW variance and precipitation maxima. A rough but quantitative estimation is next made. Acceleration of the GW packet in the latitudinal direction is written as,

$$\frac{\mathrm{d}^2 y}{\mathrm{d}t^2} \sim \frac{\mathrm{d}c_{\mathrm{g}y}}{\mathrm{d}t} = \frac{m^2}{(m^2 + k_\mathrm{h}^2)^{\frac{3}{2}}} \frac{N^2 - f^2}{(N^2 k_\mathrm{h}^2 + f^2 m^2)^{\frac{1}{2}}} \frac{\mathrm{d}k_y}{\mathrm{d}t} \tag{5}$$

$$= -\frac{k_x m^2}{(m^2 + k_\mathrm{h}^2)^{\frac{3}{2}}} \frac{N^2 - f^2}{(N^2 k_\mathrm{h}^2 + f^2 m^2)^{\frac{1}{2}}} \frac{\partial U}{\partial y}.$$

To isolate the refraction effect on the meridional propagation direction, $\mathrm{d}y/\mathrm{d}t$ is set to zero at the initial time. The zonal wind shear $\frac{\partial U}{\partial y}$ is simply set to a constant value of 4.5 m s^{-1} per 3°at 30 hPa and (160°E, 7.5°S) during the propagation (Figure 12). The latitudinal propagation distance is estimated at 28 km for GWs using $k_x \sim k_\mathrm{h} = 2\pi/(225\ \mathrm{km})$. This value is again not sufficient to explain the observed distance of ~330 km. Thus, the latitudinal propagation due to refraction is not the only mechanism to cause the difference in the latitudes between the GW variance and precipitation maxima.

5.2.4. Other possible mechanisms and a combination of multiple mechanisms

We considered other mechanisms such as advection by the southward background wind and critical level filtering at the latitudes of the precipitation maximum. However, none of them can explain the southward shift of the GW variance maximum. Meridional background wind is almost zero in the stratosphere below 3 hPa (Figure 11a) and hence cannot cause much advection. The background zonal winds are not very different between the latitudes of the GW variance and precipitation maxima (Figure 12). The eastward wind around the tropopause is rather stronger at higher latitudes (Figure 12d), which means that GWs at higher latitudes can be more effectively filtered.

In conclusion, the most important mechanism explaining the latitudinal distance about 330 km between the GW variance and precipitation maxima is the island distribution which is dense (sparse) southward (northward) of SPCZ. The selective GW excitation in the vertical shear of mean meridional wind, and the latitudinal propagation by refraction due to the latitudinal shear of mean zonal wind have secondary contribution (about 63 km in total). Probably a combination of these mechanisms is likely responsible for the latitudinal difference.

6. Summary and concluding remarks

The present study first examined the climatology and interannual variability of GW variance in the subtropical region in the summer middle stratosphere based on satellite nadir sounding data by AIRS over eight years. High-resolution temperature data at 39 km made from the *Hoffmann and Alexander* [2009] retrieval algorithm were used for the analysis. An S-transform method was applied to extract GW parameters such as temperature variance and the magnitude and direction of horizontal wavenumber. In a climatology, large GW variance is observed over continents and the tropical Maritime Continent in both hemispheres. Precipitation is also dominant over the continents but there is a systematic latitudinal difference between the GW variance maximum and precipitation maximum by about three degrees.

The interannual variability in the summer subtropics is larger in the SH than in the NH. Thus further analysis was focused on the SH. Horizontal wavelengths are longer (>200 km) over continents and the Maritime Continent and shorter (about 150 km) over the ocean. Assuming that the zonal phase speeds are opposite to the background zonal wind as is consistent with previous studies, the waves propagate primarily eastward, but the latitudinal component of the wavenumber vectors is negative (i.e., southward) for most GWs.

An interesting and important feature is that the interannual variability of the GW variance in the western and central South Pacific region in summer is closely related to the ENSO which accounts for 70% of the variation. This variation of GW variance follows the SPCZ latitudinal movement in association with the ENSO. The distribution of both horizontal wavelengths and propagation direction also vary following the ENSO. The contribution of the equatorial QBO is minor in that region.

Last but not least, we examined possible mechanisms causing the systematic latitudinal difference by 3 degrees between the maxima of GW variance and precipitation climatology. An important mechanism is the distribution of islands which are dense southward of SPCZ. It is expected that deep convection excited over islands effectively generates GWs with long vertical wavelengths, which are more easily detectable by AIRS. Selective GW excitation due to vertical shear of the upper tropospheric wind, and GW refraction in the latitudinal shear of the background wind are secondary but important mechanisms for the southward component of propagation of GWs. By using typical GW parameters estimated from AIRS data, the sum of the two mechanisms might account for about 20 % of the latitudinal distance. Combination of the three mechanisms are likely responsible for the latitudinal difference.

This study showed a significant inter-annual modulation of stratospheric GW activity by ENSO in the SH subtropical region. This fact means that the meridional circulation in the middle and upper atmosphere may be also modulated by ENSO. Changes in the meridional circulation also modify the thermal structure and affect the structure of tides, which are dominant in the upper mesosphere and thermosphere.

It is seen from comparison between Figure 3b and Figure 5d that ENSO-modulation of the GW variance is more than ten percent depending on the location. For a more quantitative discussion, it is necessary to examine the momentum flux associated with GWs. To do this, the estimation of vertical wavelengths is needed using data from at least two altitudes in addition to the temperature variance. However, generally speaking, this is difficult to derive from nadir-viewing satellite observations with low vertical resolution like

AIRS. The momentum flux is expressed using a formula $\frac{1}{2}\rho\frac{k_H}{m}\left(\frac{g}{N}\right)^2\overline{\left(\frac{T'}{T}\right)^2}$ from observed temperature variances [*Ern et al.,* 2004; *Alexander,* 2015]. Thus, we assume a typical detectable vertical wavelength of 15 km for a rough estimation. Using a climatological mean GW variance of 1 K^2, a background temperature of 250 K, a typical horizontal wavelength of 225 km, and damping due to limited vertical resolution of AIRS retrieval of about 15 % in variance [*Hoffmann and Alexander,* 2009], the climatological momentum flux observed by AIRS is estimated at about 0.5 mPa and the interannual variability related to ENSO is about 0.05 mPa. This climatological momentum flux value of the GWs observed by AIRS is comparable to the estimate (about 0.5 mPa) around the SPCZ at 40 km in January, 2006 from observations of Sounding of the Atmosphere using Broadband Emission Radiometry (SABER) and HIRDLS, which are sensitive to GWs with short vertical wavelengths unlike AIRS [*Geller et al.,* 2013].

In addition, it is also worth noting that the GW variance dependence on longitude has an interannual variability. This means that the Lagrangian mean circulation in the middle atmosphere may have significant three-dimensional structure, although it has mainly been examined in the two dimensional meridional cross section so far. It should be interesting to examine the three-dimensional structure of the interaction of GWs with the mean flow [e.g., *Kinoshita and Sato,* 2013; *Sato et al.,* 2013] and the interaction between GWs and planetary-scale waves [e.g., *Smith*, 2003; *Lieberman et al.,* 2013; *Sato and Nomoto,* 2015] in terms of interannual variability in the future.

Acknowledgments

The authors thanks Yukari N. Takayabu, Masaaki Takahashi, Tomoki Tozuka, and Hiroaki Miura for their constructive comments. This work was supported by JSPS KAKENHI Grant Numbers 25247075 and 24-2641. MJA was supported by the National Science Foundation grant numbers AGS–1318932 and AGS-1519271.

Appendix A: Noise spectra

It is expected that there are few significant GW sources such as topography, jet-front systems and convection in the winter subtropical Pacific. In addition, the background wind there is generally weak at 3 hPa and hence GWs originating from convection are not significantly Doppler shifted. Such GWs have short vertical wavelengths that are hardly detected by AIRS. Thus, we regarded the magnitude of the S-transform cross spectra of adjacent data series in such regions as "noise" spectra which is a function of the location and wavelength.

Figure A-1 shows the noise spectra obtained from adjacent two data series across the track for the region of 10°N−30°N, 150°E−120°W on February 12 and the region of 0°S−25°S, 180°W−90°W on July 12 of 2003−2011. The spectral densities, which we call variances, are larger at shorter wavelengths. At nadir where the cross track location is 0 km, the variance is maximized at a wavelength of about 30 km. Similar maxima are observed at longer wavelengths for larger distances from the nadir. Such dependence of the maximum wavelength can be explained by the coarser resolution at larger distances from the nadir. These maxima are likely due to the random noise that appears in the temperature retrievals, and hence should be removed. A weak peak is also observed around 1000 km wavelength. The reason of this peak is not clear but may be due to the detrending method used in the present study. This peak should also be removed as noise. Thus, we examined S-transform spectra in the range of wavelengths 70−700 km. Note that the variances are diminished near the edge of a cross track scan. This reflects to the cosine-shaped window function applied to the original data before the S-transform calculation. Thus the edge regions are not examined for the analysis either.

Two examples of the S-transform spectra including GW signals are shown in Figure

A-2. Figures A-2a and A-2b respectively show the results over convection in Australia on January 15, 2007 and over the Andean mountains on May 18, 2006. The latter corresponds to a significant GW event examined by *Alexander and Teitelbaum* [2011]. Clear GW signals are observed in both examples, occurring at a wavelength of 300 km and a distance of -200 km in Figure A-2a and at a wavelength near 100 km at nadir in Figure A-2b.

References

Alexander, M. J. (1998), Interpretations of observed climatological patterns in stratospheric gravity wave variance, *J. Geophys. Res.*, *103* (D8), 8627–8640, doi:10.1029/97JD03325.

Alexander, M. J. (2015), Global and seasonal variations in three-dimensional gravity wave momentum flux from satellite limb sounding temperatures, *Geophys. Res. Lett., 42,* doi:10.1002/2015GL065234.

Alexander, M. J., and C. Barnet (2007), Using satellite observations to constrain parameterizations of gravity wave effects for global models, *J. Atmos. Sci.*, *64*, 1652–1665, doi:10.1175/JAS3897.1.

Alexander, M. J., and A. W. Grimsdell (2013), Seasonal cycle of orographic gravity wave occurrence above small islands in the Southern Hemisphere: Implications for effects on the general circulation, *J. Geophys. Res. Atmos., 118*, 11,589-11,599, doi:10.1002/2013JD020526.

Alexander, M. J., and H. Teitelbaum (2007), Observation and analysis of a large amplitude mountain wave event over the Antarctic peninsula, *J. Geophys. Res., 112,* D21, doi:10.1029/2006JD008368.

Alexander, M. J., and H. Teitelbaum (2011), Three-dimensional properties of Andes mountain waves observed by satellite: A case study, *J. Geophys. Res., 116,* D23110, doi:10.1029/2011JD016151.

Alexander, M. J., J. Gille, C. Cavanaugh, M. Coffey, C. Craig, T. Eden, G. Francis, C. Halvorson, J. Hannigan, R. Khosravi, D. Kinnison, H. Lee, S. Massie, B. Nardi, J. Barnett, C. Hepplewhite, A. Lambert, and V. Dean (2008), Global estimates of gravity wave momentum flux from High Resolution Dynamics Limb Sounder observations, *J. Geophys. Res.*, *113 (D15)*, doi:10.1029/2007JD008807.

Alexander, M. J., S. D. Eckermann, D. Broutman, and J. Ma (2009), Momentum flux estimates for South Georgia Island mountain waves in the stratosphere observed via satellite, *Geophys. Res. Lett.*, *36*, L12816, doi:10.1029/2009GL038587.

Andrews, D. G., J. R. Holton, and C. B. Leovy (1987), *Middle Atmospheric Dynamics*, 489 pp., Academic Press.

Aumann, H. H., M. T. Chahine, C. Gautier, M. D. Goldberg, E. Kalnay, L. M. McMillin, H. Revercomb, and P. W. Rosenkranz (2003), AIRS/AMSU/HSB on the Aqua mission: Design, science objective, data products, and processing systems, *IEEE Trans. Geosci. Remote Sens.*, *41*, 253–264, doi:10.1109/TGRS.2002.808356.

Beres, J. H., M. J. Alexander, and J. R. Holton (2002), Effects of tropospheric wind shear on the spectrum of convectively generated gravity waves, *J. Atmos. Sci.*, *59*, 1805–1824.

Butchart, N. (2014), The Brewer-Dobson Circulation, *Rev. Geophys.*, *52*, 157-184, doi:10.1002/2013RG000448.

Dunkerton, T. J. (1984), Inertia-gravity waves in the stratosphere, *J. Atmos. Sci.*, *41*, 23, 3396-3404.

Ern, M., P. Preusse, M. J. Alexander, and C. D. Warner (2004), Absolute values of gravity wave momentum flux derived from satellite data, *J. Geophys. Res.*, *109*, D20103, doi:10.1029/2004JD004752.

Ern, M., and P. Preusse (2009), Quantification of the contribution of equatorial Kelvin waves to the QBO wind reversal in the stratosphere, *Geophys. Res. Lett., 36*, L21801, doi:10.1029/2009GL040493.

Evan, S., M. J. Alexander, and J. Dudhia (2012), WRF simulations of convectively generated gravity waves in opposite QBO phases, *J. Geophys. Res., 117,* D12117, doi:10.1029/2011JD017302.

Geller, M. A. , M. J. Alexander, P. T. Love, J. Bacmeister, M. Ern, A. Hertzog, E. Manzini, P. Preusse, K. Sato, A. A. Scaife, and T. Zhou (2013), A Comparison between Gravity Wave Momentum Fluxes in Observations and Climate Models, *J. Climate*, *26*, 6383-6405, doi:10.1175/JCLI-D-12-00545.1.

Gong, J., D. L. Wu, and S. D. Eckermann (2012), Gravity wave variances and propagation derived from AIRS radiances, *Atmos. Chem. Phys.*, *12*, 1701–1720, doi:10.5194/acp-12-1701-2012.

Hoffmann, L., and M. J. Alexander (2009), Retrieval of stratospheric temperatures from Atmospheric Infrared Sounder radiance measurements for gravity wave studies, *J. Geophys. Res.*, *114*, D07105, doi:10.1029/2008JD011241.

Hoffmann, L., X. Xue, and M. J. Alexander (2013), A global view of stratospheric gravity wave hotspots located with Atmospheric Infrared Sounder observations, *J. Geophys. Res.*, *118*, 416–434, doi:10.1029/2012JD018658.

Holton, J. R. (1983), The influence of gravity wave breaking on the general circulation of the middle atmosphere, *J. Atmos. Sci.*, *40*, 2497–2507.

Huffman, G. J., R. F. Adler, M. M. Morrissey, D. T. Bolvin, S. Curtis, R. Joyce, B. McGavock, and J. Susskind (2001), Global precipitation at one-degree daily resolution from multisatellite observations, *J. Hydrometeor.*, *2*, 36–50.

Ichikawa, H., and T. Yasunari (2008), Intraseasonal variability in diurnal rainfall over New

Guinea and the surrounding oceans during austral summer, *J. Climate*, *21*, 2852–2868, doi:10.1175/2007JCLI1784.1.

Jiang, J. H., B. Wang, K. Goya, K. Hocke, S. D. Eckermann, J. Ma, D. L. Wu, and W. G. Read (2004), Geographical distribution and interseasonal variability of tropical deep convection: UARS MLS observations and analyses, *J. Geophys. Res.*, *109*, D03111, doi:10.1029/2003JD003756.

John, S. R., and K. K. Kumar (2012), TIMED/SABER observations of global gravity wave climatology and their interannual variability from stratosphere to mesosphere lower thermosphere, *Clim. Dyn.*, *39* (6), 1489–1505, doi:10.1007/s00382-012-1329-9.

Kawatani, Y., K. Sato, T. J. Dunkerton, S. Watanabe, S. Miyahara, and M. Takahashi (2010), The Roles of Equatorial Trapped Waves and Internal Inertia–Gravity Waves in Driving the Quasi-Biennial Oscillation. Part I: Zonal Mean Wave Forcing, *J. Atmos. Sci., 67,* 963-980, doi:10.1175/2009JAS3222.1.

Kinoshita, T., and K. Sato (2013), A formulation of three-dimensional residual mean flow applicable both to inertia-gravity waves and to Rossby waves, *J. Atmos. Sci., 70,* 1577-1602, doi:10.1175/JAS-D-12-0137.1.

Lieberman, R. S., D. M. Riggin, and D. E. Siskind (2013), Stationary waves in the wintertime mesosphere: Evidence for gravity wave filtering by stratospheric planetary waves. *J. Geophys. Res. Atmos., 118,* 3139–3149, doi:10.1002/jgrd.50319.

McLandress, C., M. J. Alexander, and D. L. Wu (2000), Microwave Limb Sounder observations of gravity waves in the stratosphere: A climatology and interpretation, *J. Geophys. Res.*, *105 (D9)*, 11,947–11,967, doi:10.1029/2000JD900097.

Meyer, C. ; Hoffmann, L (2014), Validation of AIRS high-resolution stratospheric temperature retrievals, *Proc. SPIE 9242, Remote Sensing of Clouds and the Atmosphere*

XIX; and Optics in Atmospheric Propagation and Adaptive Systems XVII, 92420L, doi:10.1117/12.2066967.

Mori, S., H. Jun-Ichi, Y. I. Tauhid, M. D. Yamanaka, N. Okamoto, F. Murata, N. Sakurai, H. Hashiguchi, and T. Sribimawati (2004), Diurnal land-sea rainfall peak migration over Sumatera island, Indonesian Maritime Continent, observed by TRMM satellite and intensive rawinsonde soundings, *Mon. Wea. Rev.*, *132*, 2021–2039.

Okamoto, K., K. Sato, and H. Akiyoshi (2011), A study on the formation and trend of the Brewer-Dobson circulation, *J. Geophys. Res.*, *116*, D10117, doi:10.1029/2010JD014953.

Parkinson, C. L. (2003), Aqua: An Earth-observing satellite mission to examine water and other climate variables, *IEEE Trans. Geosci. Remote Sens.*, *41*, 173—183, doi:10.1109/TGRS.2002.808319.

Plumb, R. A. (2002), Stratospheric transport, *J. Meteorol. Soc. Japan*, *80*, 793–809.

Rienecker, M. M., M. J. Suarez, R. Gelaro, R. Todling, J. Bacmeister, E. Liu, M. G. Bosilovich, S. D. Schubert, L. Takacs, G.-K. Kim, S. Bloom, J. Chen, D. Collins, A. Conaty, A. da Silva, W. Gu, J. Joiner, R. D. Koster, R. Lucchesi, A. Molod, T. Owens, S. Pawson, P. Pegion, C. R. Redder, R. Reichle, F. R. Robertson, A. G. Ruddick, M. Sienkiewicz, and J. Woollen (2011), MERRA: NASA's Modern-Era Retrospective Analysis for Research and Applications, *J. Climate*, *24*, 3624–3648, doi:10.1175/JCLI-D-11-00015.1.

Sato, K., and T. J. Dunkerton (1997), Estimates of momentum flux associated with equatorial Kelvin and gravity waves, *J. Geophys. Res., 102,* D22, 26247-26261, doi:10.1029/96JD02514.

Sato, K., and M. Nomoto (2015), Gravity-wave induced anomalous potential vorticity gradient generating planetary waves in the winter mesosphere. *J. Atmos. Sci., 72,* 3609–

3624. doi: http://dx.doi.org/10.1175/JAS-D-15-0046.1

Sato, K., F. Hasegawa, and I. Hirota (1994), Short-period distribution in the equatorial lower stratosphere, *J. Meteor. Soc. Japan, 72,* 859-872.

Sato, K., S. Watanabe, Y. Kawatani, Y. Tomikawa, K. Miyazaki, and M. Takahashi (2009), On the origins of mesospheric gravity waves, *Geophys. Res. Lett.*, *36*, L19801, doi:10.1029/2009GL039908.

Sato, K., T. Kinoshita, and K. Okamoto (2013), A new method to estimate three-dimensional residual mean circulation in the middle atmosphere and its application to gravity-wave resolving general circulation model data, *J. Atmos. Sci., 70,* 3756–3779. doi: http://dx.doi.org/10.1175/JAS-D-12-0352.1.

Serra, Y. L., and M. J. McPhaden (2004), In situ observations of diurnal variability in rainfall over the tropical Pacific and Atlantic oceans, *J. Climate*, *17*, 3496–3509.

Smith, A. K. (2003), The origin of stationary planetary waves in the upper mesosphere. *J. Atmos. Sci., 60,* 3033‐3041.

Stephan, C., M. J. Alexander and J. Richter (2015), Characteristics of gravity waves from convection and their role in driving the Brewer-Dobson circulation. Submitted to *J. Atmos. Sci.*

Stockwell, R. G., L. Mansinha, and R. P. Lowe (1996), Localisation of the complex spectrum: The S-Transform, *IEEE Trans. Signal Process.*, *44*, 998–1001, doi:10.1109/78.492555.

Takayabu, Y. N., Spectral representation of rain profiles and diurnal variations observed with TRMM PR over the equatorial area, *Geophys. Res. Lett., 29* (12), doi:10.1029/2001GL014113, 2002.

Trenberth, K. E. (1997), The definition of El Niño. *BAMS, 78*, 2771-2777.

Tsuchiya, C., K. Sato, M. J. Alexander, and L. Hoffmann, MJO-related intraseasonal variation of gravity waves in the southern hemisphere subtropical stratosphere revealed by high-resolution AIRS observations, Submitted to *J. Geophys. Res.*

Wright, C. J., and J. C. Gille (2011), HIRDLS observations of gravity wave momentum fluxes over the monsoon regions, *J. Geophys. Res.*, *116*, D12103, doi:10.1029/2011JD015725.

Wu, D. L., and J. W. Waters (1996), Satellite observations of atmospheric variances: A possible indication of gravity waves, *Geophys. Res. Lett.*, *23*, 3631–3634, doi:10.1029/96GL02907.

Zhang, Y., J. Xiong, L. Liu, and W. Wan (2012), A global morphology of gravity wave activity in the stratosphere revealed by the 8-year SABER/TIMED data, *J. Geophys. Res.*, *117*, D21101, doi:10.1029/2012JD017676.

Figure captions

Figure 1. (a) The angle α between the directions of the data series across and along the satellite orbit at the daytime (ascending orbit) shown by a red curve and at the nighttime (descending orbit) by a blue curve as a function of the latitude, calculated using data on December 24, 2003. (b) A schematic illustration of a wave phase structure and directions along and across the satellite track. See text for details.

Figure 2. (a) DJF mean climatology of GW variance at a height of 39 km binned with an interval of 2.5° latitude and 10° longitude made from eight years from 2003/04−2010/11 in the SH subtropics. (b) The same as (a) but for JJA mean climatology from 2003−2011 in the NH subtropical region. (c) ((d)) Standard deviation of the DJF (JJA) GW variance for the eight (nine) years. Black contours show mean zonal winds at 3 hPa at an interval of 10 m s^{-1}.

Figure 3. DJF mean climatology of (a) precipitation (color), zonal wind at 100 hPa (contours at an interval of 5 m s^{-1}), (b) GW variance at 39 km (color), zonal wind at 3 hPa (contours at an interval of 5 m s^{-1}), (c) horizontal wavelengths averaged with a weight of the GW variance, (d) direction of the horizontal wavenumber vector averaged with a weight of the GW variance shown by angles counter-clockwise from the eastward direction. The thick red curve denotes the latitude of the climatological precipitation maxima for 150°E−140°W. The longitudinal region of 160°E−160°W for which a scatter diagram analysis is made (Figure 10b) is denoted by two vertical thick lines.

Figure 4. Time series of SST anomaly from the 30-year climatology in the NINO.3 region (5°S−5°N, 150°W− 90°W). Black dots show NINO.3 data used for the regression analysis. See text for details.

Figure 5. Maps of correlation coefficients of NINO.3 time series with (a) DJF-mean

precipitation and (b) GW variance. Red (blue) contours show positive (negative) correlation. Thin contours show ± 0.62 corresponding to the 90 % significant level and thick contours show ± 0.83 corresponding to the 99 % significant level. Regression coefficients for (c) DJF-mean precipitation and (d) GW variance are shown by colors only in regions with correlation coefficient magnitudes larger than 0.62. Thick black lines show the regions of (A) the equatorial central South Pacific (from 150°E to 150°W, from 0°S to 10°S), (B) and (C) the regions respectively to the east and west of SPCZ (from 150°E to 110°W, from 10°S to 30°S). The SPCZ is denoted by a thick red curve.

Figure 6. DJF-mean time series of precipitation (blue), GW variance (black), and zonal wind at 3 hPa (green) for (a) the equatorial central South Pacific, and the regions (b)-west and (c) east of the SPCZ. These regions are shown in Figure 5 as thick black lines.

Figure 7. The same as Figure 5 but for ((a) and (c)) horizontal wavelengths averaged with a weight of the GW variance and ((b) and (d)) direction of horizontal wavenumber vector averaged with a weight of the GW variance.

Figure 8. Composites of the GW variance (black), precipitation (blue), and mean ocean fraction (green) at longitudes from 150°E−150°W as a function of the latitude relative to the climatological SPCZ. (a) Composites are made for the climatology. (b) Composites are made for the seasonal mean in the El Niño years such as 2003/2004, 2004/2005, 2006/2007, and 2009/2010. (c) The same as (b) but for the La Niña years such as 2005/2006, 2007/2008, 2008/2009, and 2010/2011.

Figure 9. (a) Correlation coefficients of DJF-mean GW variance with the DJF-mean zonal mean zonal wind at 10 hPa at the equator (QBO time series). Positive (negative) values are shown by red (blue) contours. Thin contours show ± 0.62 (a significant level of 90%) and a thick contours show ± 0.83 (a significant level of 99%). (b) Regression

coefficients of DJF-mean GW variance to the QBO time series are shown by colors only in the regions where the correlation coefficient magnitudes are larger than 0.62.

Figure 10. (a) A map of mean ocean fraction from MERRA. (b) Histogram and contours for the precipitation versus the GW variance at 39 km in the region of (160°E−160°W, 0°−20°S). Contour interval is 2. (c) Mean ocean fraction as a function of precipitation and the GW variance at 39 km for the same region as for (b).

Figure 11. A composite latitude and height cross section of (a) the mean meridional wind at a contour interval of 0.5 m s^{-1}. Composite latitudinal profiles of (b) precipitation and (c) GW variance averaged for 160°E−160°W. The reference latitude is the latitude of the precipitation maximum between 0°−30°S.

Figure 12. Latitude and height cross sections of background zonal winds at (a) 160°E and (d) 160°W. Contour intervals are 2.5 m s^{-1}. Latitudinal distributions of the precipitation at (b) 160°E and (e) 160°W and those of GW variance at (c) 160°E and (f) 160°W. Thin vertical lines denote the latitudes of the maximum precipitation ((b) and (e)) and the maximum GW variance ((c) and (f)).

Figure A-1. Noise spectra calculated for the winter subtropics using an S-transform method. See the text for details. Contour intervals are 2.5 dB. Wave characteristics are estimated for the region surrounded by four thin blue lines.

Figure A-2. Examples of the S-transform cross spectra in which GW signals are observed: (a) in Australia on January 15, 2007 and (b) over the Andes on May 8, 2006. Displayed are the magnitude of cross spectra (dB). Contour intervals are 5 dB. Only contours of larger values than -15 dB with the same unit for Figure A-1 are shown.

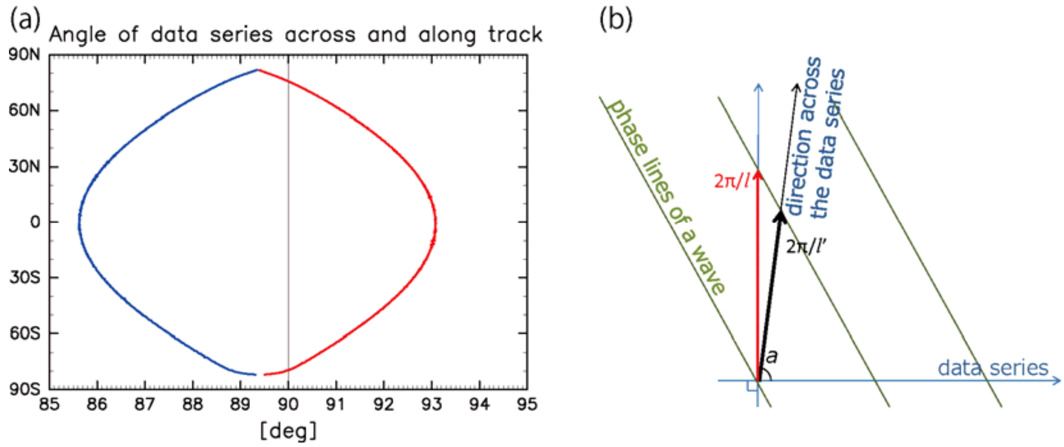

Figure 1. (a) The angle a between the directions of the data series across and along the satellite orbit at the daytime (ascending orbit) shown by a red curve and at the nighttime (descending orbit) by a blue curve as a function of the latitude, calculated using data on December 24, 2003. (b) A schematic illustration of a wave phase structure and directions along and across the satellite track. See text for details.

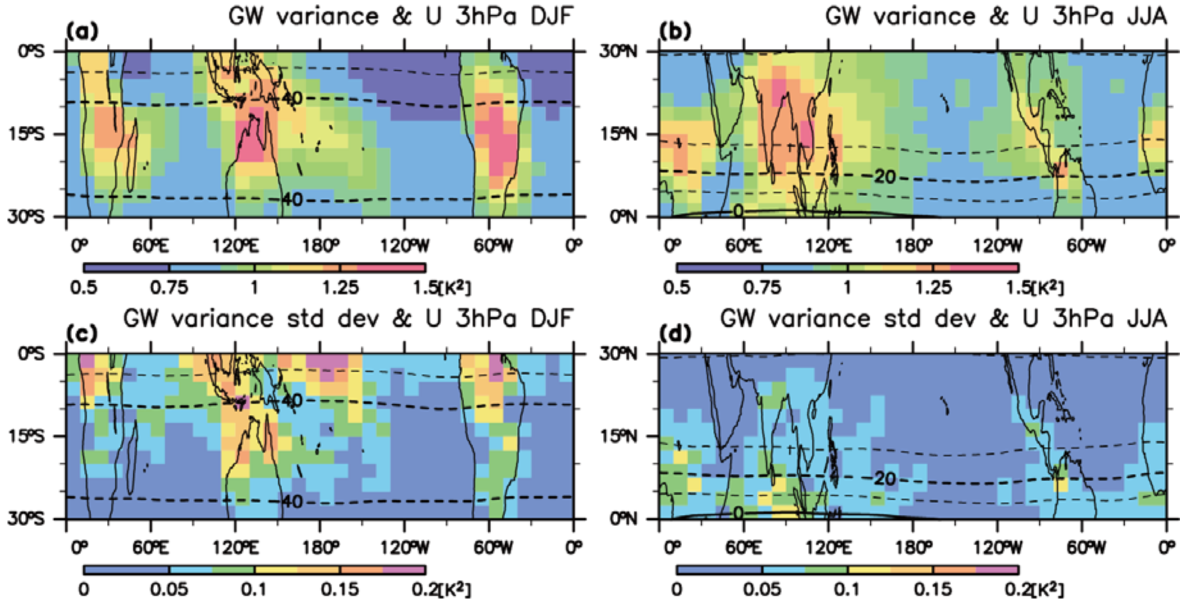

Figure 2. (a) DJF mean climatology of GW variance at a height of 39 km binned with an interval of 2.5° latitude and 10° longitude made from eight years from 2003/04−2010/11 in the SH subtropics. (b) The same as (a) but for JJA mean climatology from 2003−2011 in the NH subtropical region. (c) ((d)) Standard deviation of the DJF (JJA) GW variance for the eight (nine) years. Black contours show mean zonal winds at 3 hPa at an interval of 10 m s^{-1}.

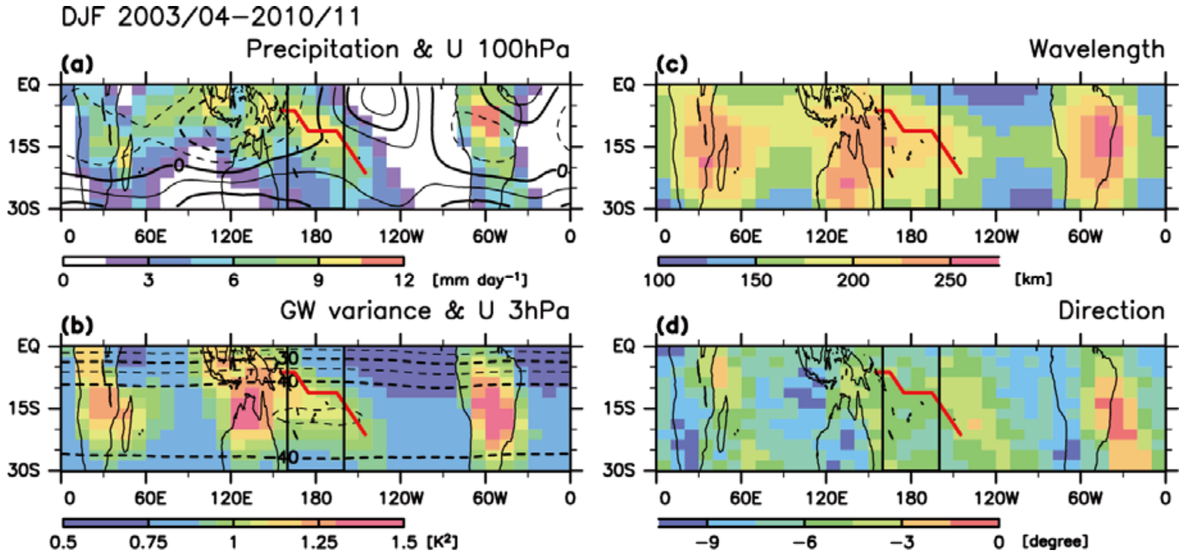

Figure 3. DJF mean climatology of (a) precipitation (color), zonal wind at 100 hPa (contours at an interval of 5 m s^{-1}), (b) GW variance at 39 km (color), zonal wind at 3 hPa (contours at an interval of 5 m s^{-1}), (c) horizontal wavelengths averaged with a weight of the GW variance, (d) direction of the horizontal wavenumber vector averaged with a weight of the GW variance shown by angles counter-clockwise from the eastward direction. The thick red curve denotes the latitude of the climatological precipitation maxima for 150°E−140°W. The longitudinal region of 160°E−160°W for which a scatter diagram analysis is made (Figure 10b) is denoted by two vertical thick lines.

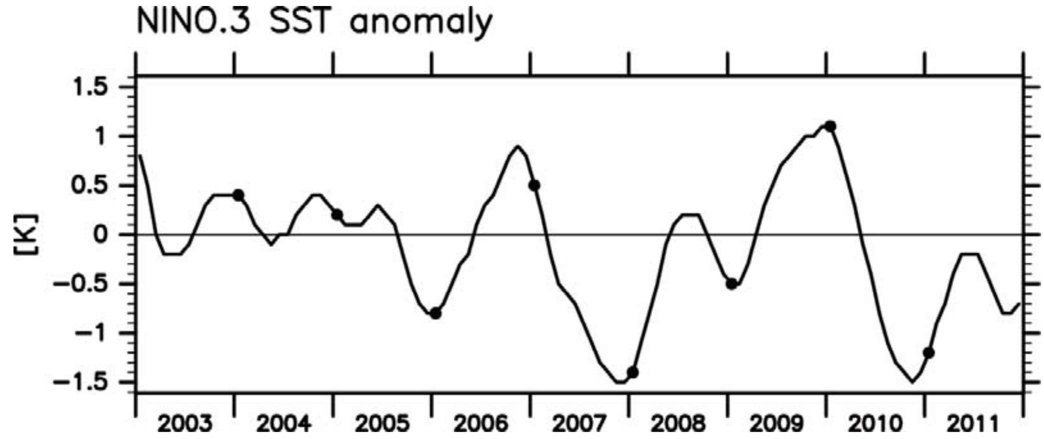

Figure 4. Time series of SST anomaly from the 30-year climatology in the NINO.3 region (5°S−5°N, 150°W− 90°W). Black dots show NINO.3 data used for the regression analysis. See text for details.

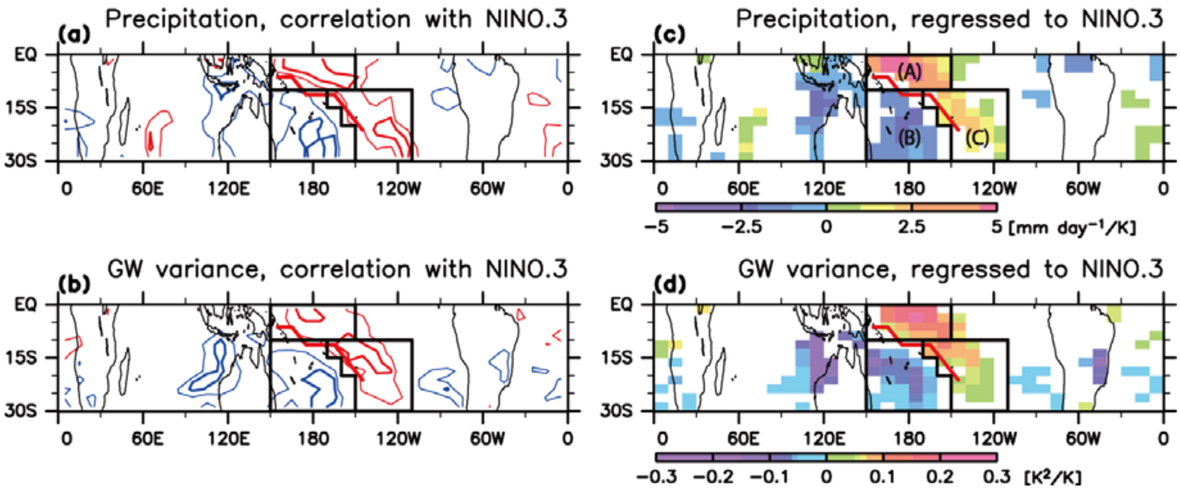

Figure 5. Maps of correlation coefficients of NINO.3 time series with (a) DJF-mean precipitation and (b) GW variance. Red (blue) contours show positive (negative) correlation. Thin contours show ± 0.62 corresponding to the 90 % significant level and thick contours show ± 0.83 corresponding to the 99 % significant level. Regression coefficients for (c) DJF-mean precipitation and (d) GW variance are shown by colors only in regions with correlation coefficient magnitudes larger than 0.62. Thick black lines show the regions of (A) the equatorial central South Pacific (from 150°E to 150°W, from 0°S to 10°S), (B) and (C) the regions respectively to the east and west of SPCZ (from 150°E to 110°W, from 10°S to 30°S). The SPCZ is denoted by a thick red curve.

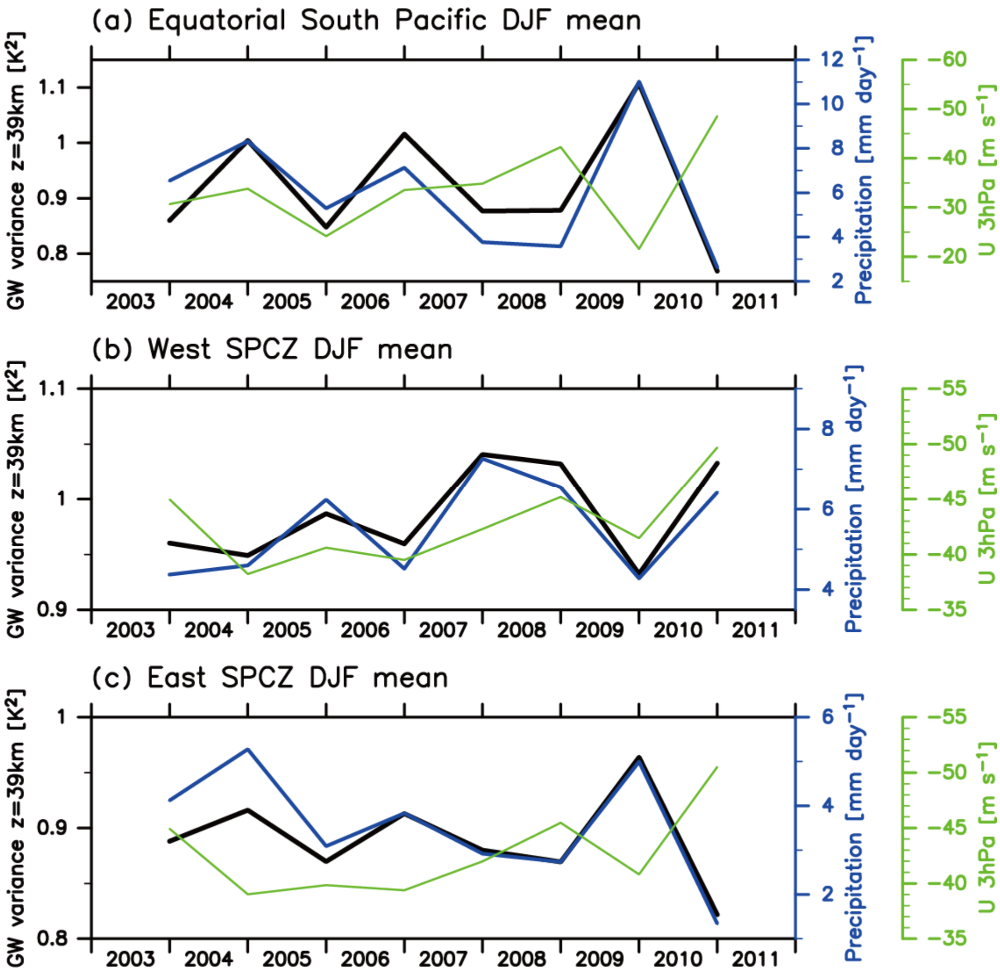

Figure 6. DJF-mean time series of precipitation (blue), GW variance (black), and zonal wind at 3 hPa (green) for (a) the equatorial central South Pacific, and the regions (b) west and (c) east of the SPCZ. These regions are shown in Figure 5 as thick black lines.

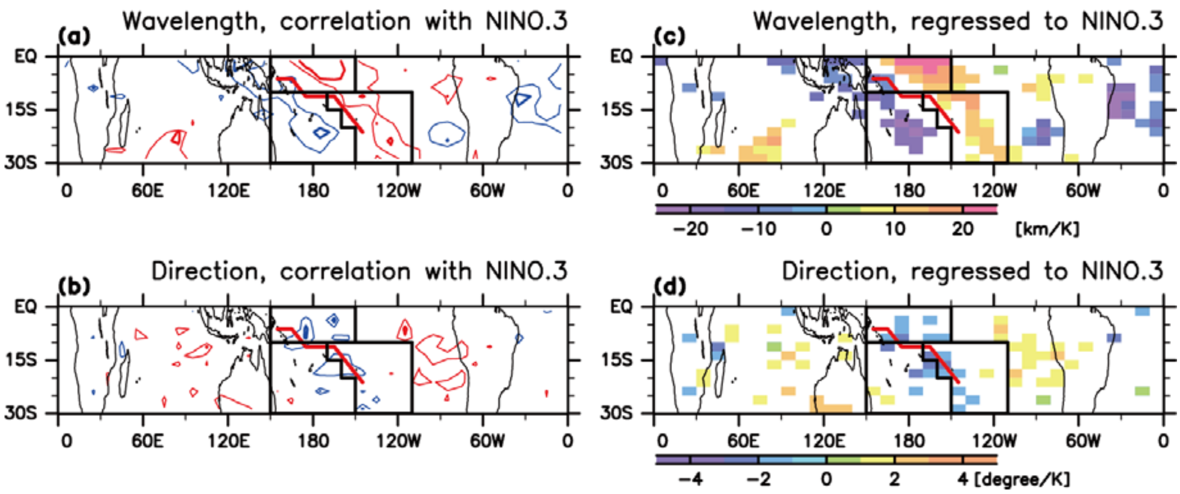

Figure 7. The same as Figure 5 but for ((a) and (c)) horizontal wavelengths averaged with a weight of the GW variance and ((b) and (d)) direction of horizontal wavenumber vector averaged with a weight of the GW variance.

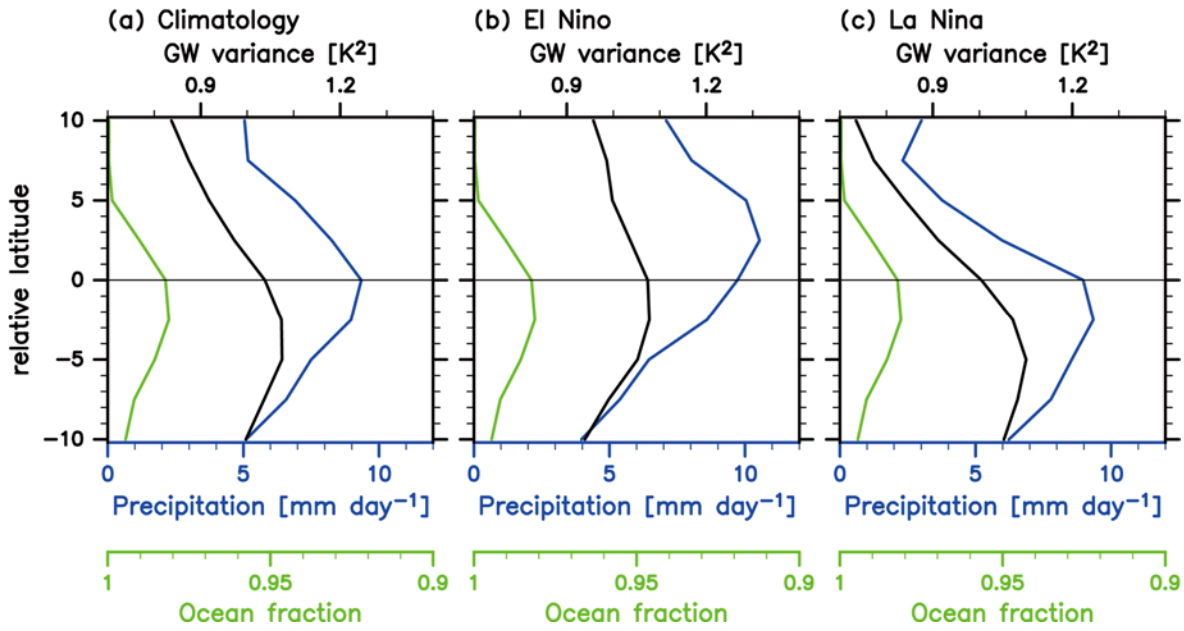

Figure 8. Composites of the GW variance (black), precipitation (blue), and mean ocean fraction (green) at longitudes from 150°E−150°W as a function of the latitude relative to the climatological SPCZ. (a) Composites are made for the climatology. (b) Composites are made for the seasonal mean in the El Niño years such as 2003/2004, 2004/2005, 2006/2007, and 2009/2010. (c) The same as (b) but for the La Niña years such as 2005/2006, 2007/2008, 2008/2009, and 2010/2011.

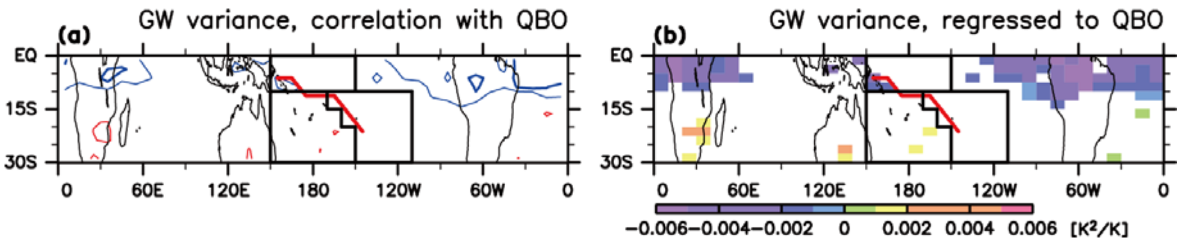

Figure 9. (a) Correlation coefficients of DJF-mean GW variance with the DJF-mean zonal mean zonal wind at 10 hPa at the equator (QBO time series). Positive (negative) values are shown by red (blue) contours. Thin contours show ± 0.62 (a significant level of 90%) and a thick contours show ± 0.83 (a significant level of 99%). (b) Regression coefficients of DJF-mean GW variance to the QBO time series are shown by colors only in the regions where the correlation coefficient magnitudes are larger than 0.62.

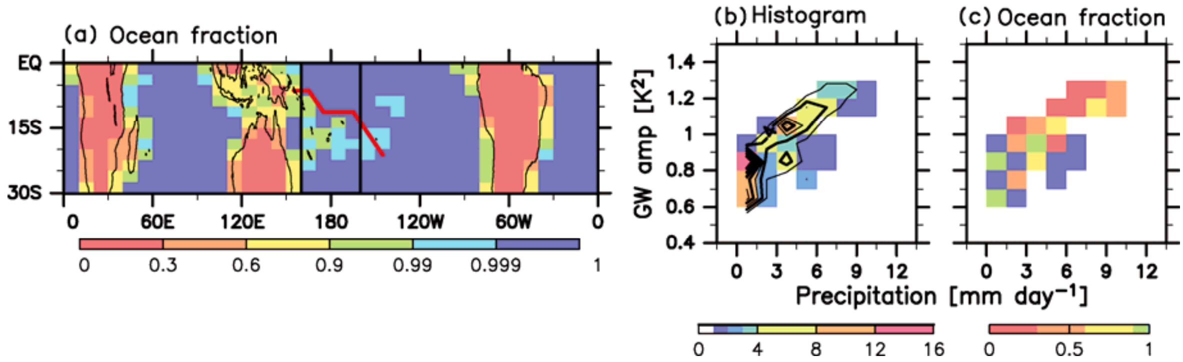

Figure 10. (a) A map of mean ocean fraction from MERRA. (b) Histogram and contours for the precipitation versus the GW variance at 39 km in the region of (160°E−160°W, 0°−20°S). Contour interval is 2. (c) Mean ocean fraction as a function of precipitation and the GW variance at 39 km for the same region as for (b).

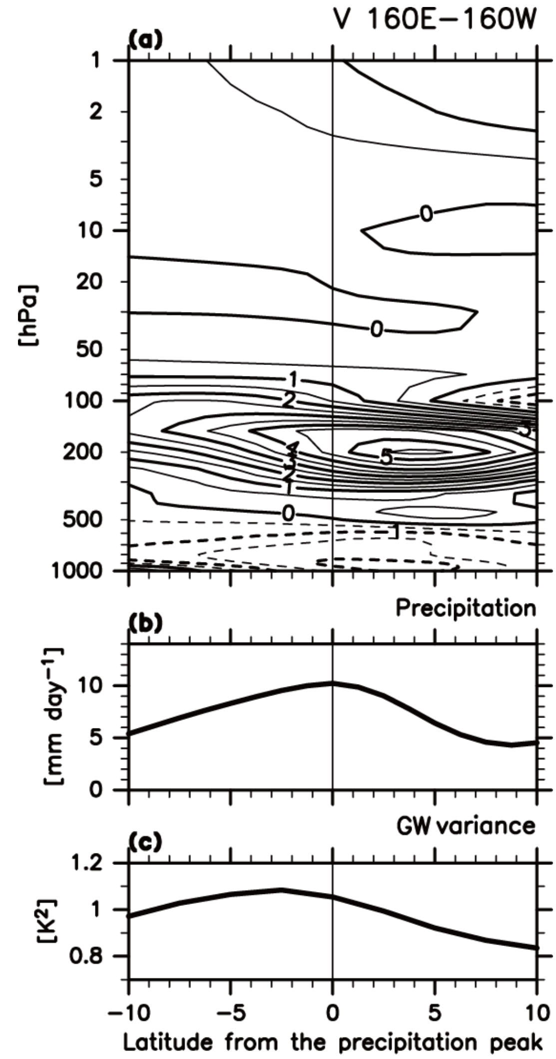

Figure 11. A composite latitude and height cross section of (a) the mean meridional wind at a contour interval of 0.5 m s^{-1}. Composite latitudinal profiles of (b) precipitation and (c) GW variance averaged for 160°E−160°W. The reference latitude is the latitude of the precipitation maximum between 0°−30°S.

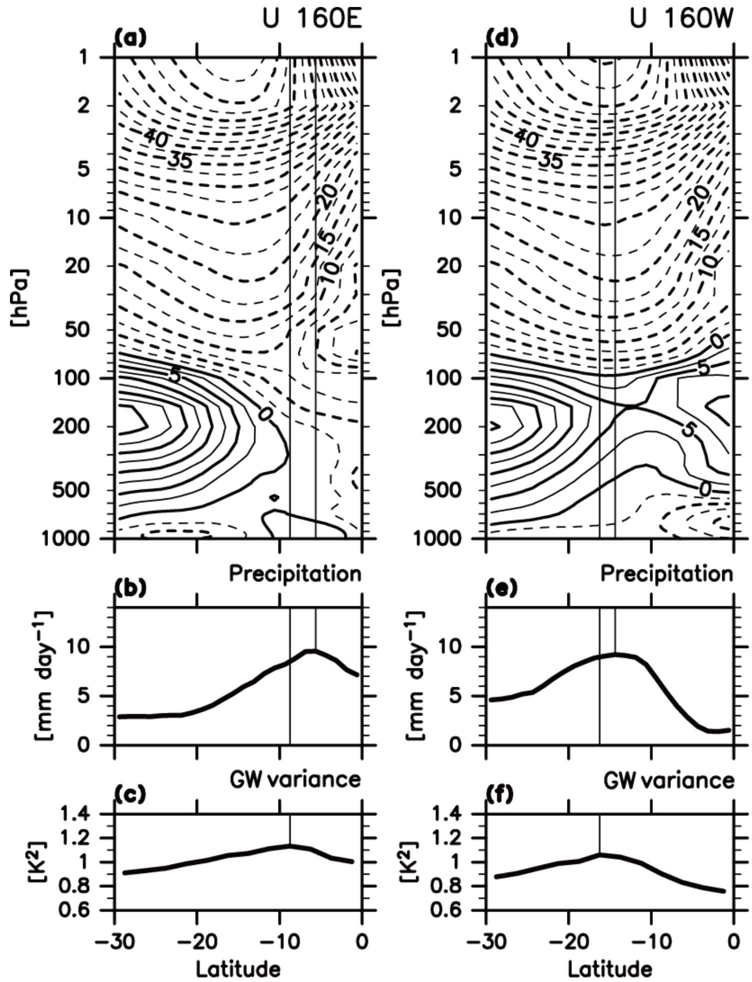

Figure 12. Latitude and height cross sections of background zonal winds at (a) 160°E and (d) 160°W. Contour intervals are 2.5 m s^{-1}. Latitudinal distributions of the precipitation at (b) 160°E and (e) 160°W and those of GW variance at (c) 160°E and (f) 160°W. Thin vertical lines denote the latitudes of the maximum precipitation ((b) and (e)) and the maximum GW variance ((c) and (f)).

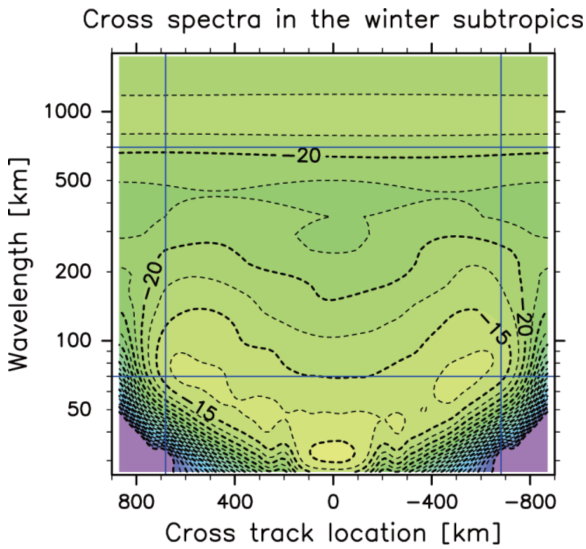

Figure A-1. Noise spectra calculated for the winter subtropics using an S-transform method. See the text for details. Contour intervals are 2.5 dB. Wave characteristics are estimated for the region surrounded by four thin blue lines.

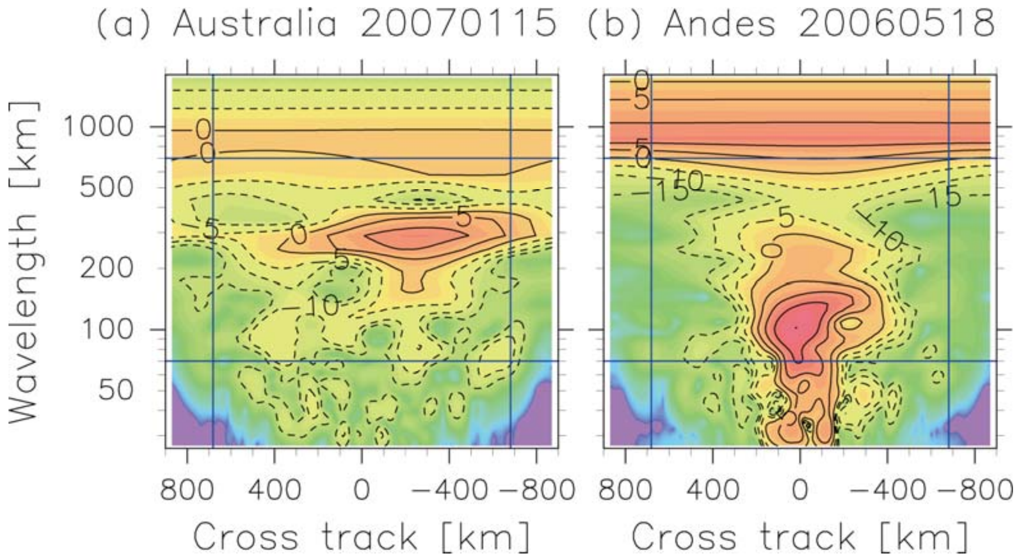

Figure A-2. Examples of the S-transform cross spectra in which GW signals are observed: (a) in Australia on January 15, 2007 and (b) over the Andes on May 8, 2006. Displayed are the magnitude of cross spectra (dB). Contour intervals are 5 dB. Only contours of larger values than -15 dB with the same unit for Figure A-1 are shown.